ACS NANO

Open Access

This article is licensed under CC-BY-NC-ND 4.0

www.acsnano.org

Article

Nanocavity-Mediated Purcell Enhancement of Er in TiO_2 Thin Films Grown via Atomic Layer Deposition

Cheng Ji, Michael T. Solomon, Gregory D. Grant, Koichi Tanaka, Muchuan Hua, Jianguo Wen, Sagar Kumar Seth, Connor P. Horn, Ignas Masiulionis, Manish Kumar Singh, Sean E. Sullivan, F. Joseph Heremans, David D. Awschalom, Supratik Guha,* and Alan M. Dibos*

Cite This: *ACS Nano* 2024, 18, 9929−9941

Read Online

ACCESS | Metrics & More | Article Recommendations | Supporting Information

ABSTRACT: **The use of trivalent erbium (Er^{3+}), typically embedded as an atomic defect in the solid-state, has widespread adoption as a dopant in telecommunication devices and shows promise as a spin-based quantum memory for quantum communication. In particular, its natural telecom C-band optical transition and spin-photon interface make it an ideal candidate for integration into existing optical fiber networks without the need for quantum frequency conversion. However, successful scaling requires a host material with few intrinsic nuclear spins, compatibility with semiconductor foundry processes, and straightforward integration with silicon photonics. Here, we present Er-doped titanium dioxide (TiO_2) thin film growth on silicon substrates using a foundry-scalable atomic layer deposition process with a wide range of doping controls over the Er concentration. Even though the as-grown films are amorphous after oxygen annealing, they exhibit relatively large crystalline grains, and the embedded Er ions exhibit the characteristic optical emission spectrum from anatase TiO_2. Critically, this growth and annealing process maintains the low surface roughness required for nanophotonic integration. Finally, we interface Er ensembles with high quality factor Si nanophotonic cavities via evanescent coupling and demonstrate a large Purcell enhancement (≈300) of their optical lifetime. Our findings demonstrate a low-temperature, nondestructive, and substrate-independent process for integrating Er-doped materials with silicon photonics. At high doping densities this platform can enable integrated photonic components such as on-chip amplifiers and lasers, while dilute concentrations can realize single ion quantum memories.**

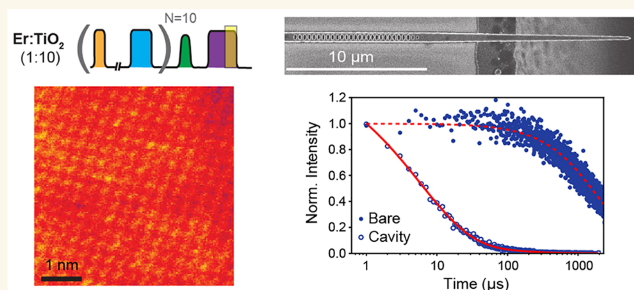

KEYWORDS: *Atomic layer deposition, Nanophotonics, Rare-earth ions, Purcell enhancement, Quantum memory*

Future quantum networks may bring tremendous improvement to realms of secure communication, distributed quantum computing, and remote quantum sensing.[1] In order for quantum networks to achieve reliable information transfer over long distances with suitable bandwidth, the network nodes must eventually employ quantum repeaters to overcome lossy single photon channels.[2−5] Trivalent erbium (Er^{3+} or Er for brevity) is a workhorse emitter used in traditional telecommunications technology, and Er ions have recently emerged as promising communication qubits due to their narrow telecom C-band optical transition[6,7] and long electron spin coherence times.[8−10] Individual Er ions have already shown promise as a quantum memory element in repeaters, demonstrating storage via the spin state for use in future entanglement swapping protocols.[11−13] In addition, photonics-integrated ensembles of Er ions have also been applied in microwave-to-optical quantum state transduction,[14−16] to address the challenge of interfacing the optical photons used in quantum networks (∼195 THz) with processing nodes operating at microwave frequencies (∼10 GHz). However, despite these benefits, the long-lived optical lifetime of the telecom C-band transition has limited its development as nanophotonic cavities are necessary to enhance light−matter interactions and greatly decrease the photon excited state lifetime via Purcell

Received: October 11, 2023
Revised: February 20, 2024
Accepted: February 28, 2024
Published: March 27, 2024

Downloaded via UNIV OF CHICAGO on September 4, 2024 at 19:09:04 (UTC).
See https://pubs.acs.org/sharingguidelines for options on how to legitimately share published articles.

© 2024 UChicago Argonne, LLC, Operator of Argonne National Laboratory. Published by American Chemical Society

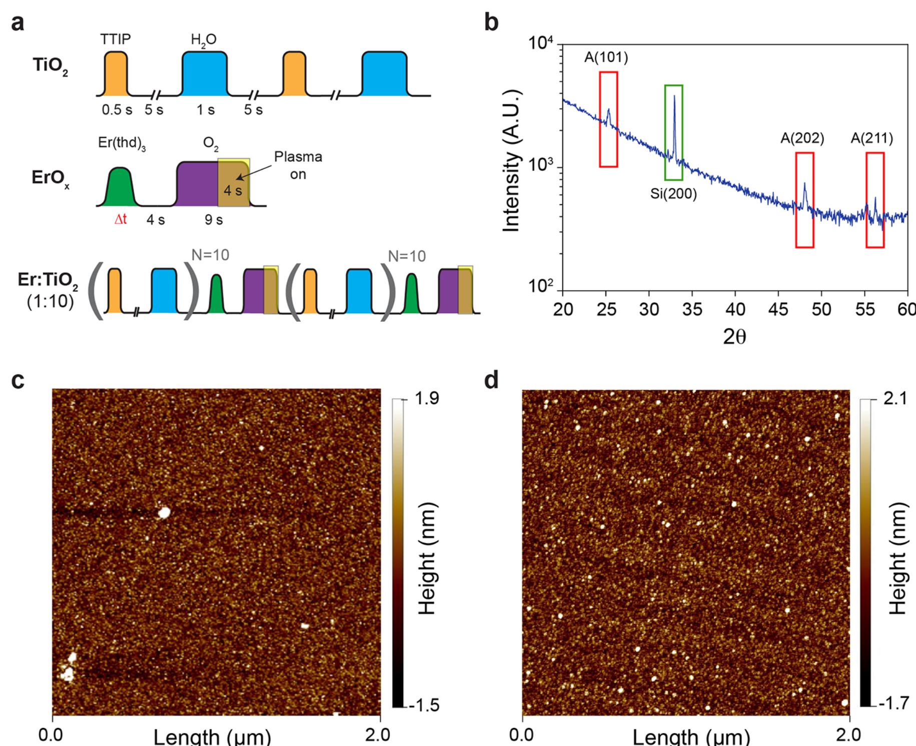

Figure 1. ALD process and material characterization. (a) ALD deposition process pulse sequence. Top (TiO_2): Two cycles of thermal ALD growth are conducted, where the TTIP precursor and water are successively pulsed into the chamber and reacted to form a TiO_2 monolayer. Middle (ErO_x): A single cycle where $Er(thd)_3$ is pulsed into the chamber with a bubbler and a turbo pump is used to remove excess precursor. The residual precursor reacts with oxygen plasma, which is turned on during the last 4 s of the oxygen pulse, to create a layer of erbium oxide. The $Er(thd)_3$ pulse length (Δt, marked in red) can be varied to control the doping level. Bottom (Er:TiO_2): Composite growth, where one ErO_x deposition cycle is followed by 10 cycles of TiO_2 deposition to space out the Er ions. The doping concentration can be further controlled by adjusting the $Er(thd)_3$ evaporation temperature and pulse length. (b) XRD spectrum of an oxygen annealed Er-doped TiO_2 thin film grown on a Si(100) substrate. The thin film comprises a "10/10/10" structure, as described in the main text. The XRD spectrum highlights the characteristic peaks of anatase TiO_2 in the red boxes and the peak from the Si substrate in the green box. (c, d) AFM height scans of (c) as-grown and (d) annealed thin films from the same growth run. The AFM scan area measures 2 μm × 2 μm. The root-mean-square roughness (R_q) and arithmetic mean roughness (R_a) values for (c) are 0.522 and 0.348 nm, respectively. The R_a and R_q values for (d) are 0.520 and 0.399 nm, respectively.

enhancement. Beyond quantum applications, successful integration of Er with silicon photonics can reduce the device footprint and reduce power requirements for classical telecommunications devices,[17] such as frequency synthesizers,[18] modulators,[19] on-chip optical gain media for light sources,[20,21] and integrated telecom amplifiers.[22] Thus, regardless of application, there is an emerging need for scalable, foundry-compatible growth techniques, which exhibit large dopant tunability, and fabrication processes that integrate these materials into on-chip photonic platforms.

To address the challenges in integrating silicon photonics with functional Er-doped materials for quantum networking nodes, recent studies have demonstrated enhanced emission and control of a single Er ion via flip-chip bonded silicon nanophotonic cavities on the surface of solid-state Er-doped bulk crystals.[23−25] However, to be scalable at the foundry-level, it is highly preferable to couple Er to on-chip nanophotonic cavities via the growth and patterning of Er-doped films using well-established semiconductor processes. This is most easily achieved by doping Er ions in a suitable host material that is compatible with nanophotonic platforms such as silicon-on-insulator (SOI).[26−28] Previous studies with SOI-based photonics have used ion implantation[27,28] to directly embed Er into Si devices or molecular beam deposition[26] to grow thin-film Er-doped crystals on top of SOI (followed by fabrication of nanophotonic cavities). There have been recent demonstrations of wafer-scale crystalline hexagonal boron nitride (hBN) for flexible heterointegration on a variety of substrates for the creation of photonic devices.[29] If combined with rare earth ion implantation into the hBN layer,[30] the resultant doped crystal could also be transferred onto a suitable photonic substrate to create a hybrid rare-earth nanophotonic platform. While both ion implantation and molecular beam deposition techniques are effective, they have drawbacks. Ion implantation is relatively straightforward, but the large Er ion mass can lead to excessive lattice damage upon impact, creating interstitial sites and deleterious decay pathways. The crystalline damage is often difficult to fully repair, even after high temperature annealing. In contrast, molecular beam deposition with in situ Er doping can produce high-quality thin films, but it is expensive, needs to be performed in ultra-high vacuum, and growth parameters are highly dependent on the substrate. Overall these complexities make foundry-level processing quite challenging and prevent the integration of various active components with photonic circuits at scale.

An alternative approach enabling such integration is to grow high-quality thin films via atomic layer deposition (ALD), a low-temperature, nondestructive, and substrate-independent process. ALD offers significant advantages over molecular beam epitaxy as a manufacturing method for a variety of

https://doi.org/10.1021/acsnano.3c09878
ACS Nano 2024, 18, 9929−9941

reasons including scalability, throughput, cost of operation, deposition conformality, and thin film uniformity; and as a result, ALD is already ubiquitous in the semiconductor industry.[31−35] In ALD, gaseous chemical precursors react on the substrate surface in a layer-by-layer deposition process, with excess precursors and byproducts purged out between each reaction step. This process allows for cyclic layer-by-layer deposition, offering precise control over the film thickness and conformality. Studies on Er-doped dielectric oxides grown by ALD have been sparse, though ALD-grown Er-doped Al_2O_3 thin films have been used for on-chip nanolasers[20] and have shown potential for integration with waveguides.[21] However, the reported optical line width in amorphous aluminum oxide has been too broad for quantum communication applications. To address this limitation, titanium dioxide (TiO_2) has been proposed as a desirable host material because it has a low natural abundance of intrinsic nuclear spins minimizing decoherence and a relatively large optical bandgap.[36−38] Experimental demonstrations have shown narrow ensemble optical and spin line widths for erbium when implanted into bulk rutile phase TiO_2, albeit after high temperature annealing.[39] Reasonably narrow inhomogeneous optical line widths have also been achieved with molecular beam epitaxy of thin film single crystal anatase TiO_2 on $LaAlO_3$ substrates.[40]

Recently we presented preliminary results on low temperature ALD growth of Er-doped TiO_2 thin films, which were directly deposited on Si and annealed.[41] Our characterization included the crystalline phase, surface roughness, and inhomogeneous line width via X-ray diffraction (XRD), atomic force microscopy (AFM), and photoluminescence excitation (PLE) spectroscopy, respectively. In this Article, we expound on these results by investigating the anatase phase TiO_2 crystalline material that emerges after annealing. We determine the large grain size and crystallinity by using electron microscopy and characterize the large range of Er doping via secondary ion mass spectrometry (SIMS). With a better understanding of the material quality, we demonstrate the applicability of ALD grown films to nanophotonic devices by fabricating and measuring 1D photonic crystal cavities using Er:TiO_2 grown on SOI wafers. Our findings suggest that Er:TiO_2 thin films synthesized via ALD and integrated with silicon photonics provide a scalable, foundry-compatible growth technique that exhibits large dopant tunability able to meet the emerging needs of both classical and quantum technologies.

RESULTS AND DISCUSSION

Er-Doped Thin-Film TiO_2 Growth. The Er-doped TiO_2 thin films were grown by using a plasma-enhanced ALD system, which can be operated with and without plasma. The deposition process involved the use of titanium isopropoxide (TTIP) and water (H_2O) as precursors for the thermal deposition of TiO_2 (additional growth details are discussed in Methods).[42−44] We chose TTIP as the Ti precursor to minimize impurities in the as-grown TiO_2 thin films because of its composition, which comprises only elements of carbon, hydrogen, titanium, and oxygen.[45] For the Er doping, we selected tris(2,2,6,6-tetramethyl-3,5-heptanedionato)erbium ($Er(thd)_3$ or $Er(tmhd)_3$), as it can react with oxygen plasma to form atomic layers of erbium oxides, thereby incorporating erbium into various host materials.[20,46−49] In an effort to grow smooth films, we deliberately maintained the Si substrates at a temperature of 120 °C during the deposition, well below the 150−165 °C temperature range for deposition of the anatase phase TiO_2,[50] at the expense of amorphous growth.[42]

The Er:TiO_2 ALD pulse sequence is depicted schematically in Figure 1a. Similar in overall sequence to that demonstrated for Er:Al_2O_3,[20] we employ an alternating sequence of undoped TiO_2 layers interrupted with single cycles of ErO_x to provide the Er doping. For the undoped thermal ALD TiO_2 deposition steps (Figure 1a, top), we pulse the TTIP precursor into the chamber for 0.5 s and the water for 1 s, where the additional H_2O pulse time is used to fully consume the TTIP. We use a 5 s window after each pulse to pump out excess precursor, thereby allowing for a more homogeneous deposited layer. For the Er doping process, we introduce $Er(thd)_3$ into the chamber via a bubbler where it binds to the substrate (Figure 1a, middle). The $Er(thd)_3$ pulse length is variable (Δt), to coarsely control the Er concentration. Following a 4 s wait time, we pulse molecular oxygen into the chamber and, synchronously, we open a turbo molecular pumping line to quickly remove excess precursors. After 5 s of O_2 flow, we ignite the oxygen plasma for 4 s, reacting with the $Er(thd)_3$ on the surface to form atomic layers of erbium oxide. Upon plasma cessation, we close the valve to the turbo pump, completing one cycle of ErO_x deposition. In this study, the growth cycle ratio was fixed at 1 cycle of ErO_x for every 10 cycles of TiO_2, as delineated in the lower panel of Figure 1a. After the deposition, we remove the sample from the reactor and perform ex situ thermal annealing at 400 °C for 30 min in a pure oxygen environment.

We can make use of two primary methods to control the concentration of dopants during ALD growth: (1) altering the TiO_2 deposition ratio relative to ErO_x deposition, or (2) controlling the growth rate of the ErO_x layer itself. In the first approach, the overall Er concentration is controlled by modifying the TiO_2 spacing (via insertion of more cycles of TTIP/H_2O) around each ErO_x layer. However, this method, while feasible and easy to apply in ALD processes, has a limited tuning range from a few percent to a few tenths of a percent due to the finite number of cycles required to grow a thin film. In this study, we focused on the second method of controlling doping by tuning the erbium oxide deposition rate. For example, to decrease the Er concentration, we can lower the $Er(thd)_3$ evaporation temperature and shorten the precursor pulse. Consequently, in each cycle, a reduced amount of $Er(thd)_3$ enters the reaction chamber.

Morphology and Doping Characterization. Previous optical experiments have shown that the inclusion of undoped "buffer" and "capping" layers can reduce optical inhomogeneous broadening for epitaxial Er:Y_2O_3 films,[51] epitaxial Er:TiO_2 films,[40] as well as spectral diffusion and inhomogeneous line width broadening for Er in polycrystalline TiO_2 films.[52] While a thicker layer is better for optical properties, it is more difficult to etch for eventual nanophotonic devices. With both of these considerations in mind, the films used for our optical studies were grown with a "10/10/10" doped heterostructure: a 10 nm undoped TiO_2 buffer layer at the Si interface, a 10 nm Er-doped TiO_2 layer in the middle, and a 10 nm undoped TiO_2 capping layer on top. Figure 1b displays the XRD spectrum of an oxygen annealed "10/10/10" heterostructure thin film sample. The spectrum shows the characteristic peaks of anatase TiO_2[53] (marked with red boxes), though the signature is weak due to the modest thickness of the film, as well as the peak from the Si substrate (green box).[54] The oxygen annealing process enhances the polycrystallinity of the as-grown amorphous film, as has been seen previously.[55] To

https://doi.org/10.1021/acsnano.3c09878
ACS Nano 2024, 18, 9929−9941

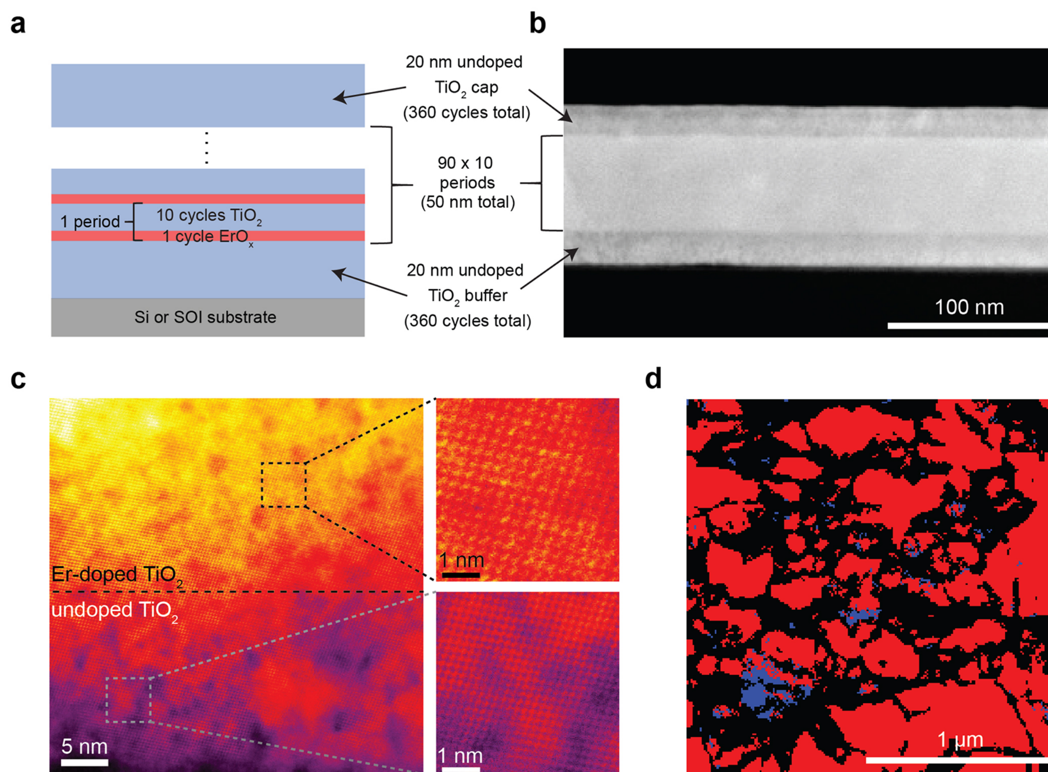

Figure 2. Electron microscopy of Er-doped thin films. (a) Schematic diagram of the "20/50/20" doped heterostructure used for SIMS elemental analysis and electron microscopy, consisting of a 20 nm undoped TiO_2 buffer layer, a 50 nm Er-doped TiO_2 layer, and a 20 nm pure TiO_2 capping layer. The thin film is grown on Si(100) or SOI. A thinner "10/10/10" heterostructure with the same 1 ErO_x to 10 TiO_2 layer ratio is used in the doped region for optical experiments. (b) A low magnification high-angle annular dark-field scanning transmission electron microscopy (HAADF-STEM) image of a sample cross-section with an Er doping level of 2950 ppm after oxygen annealing. (c) A high magnification HAADF-STEM image with false color heat map of the same annealed sample as in (b) and focused on the lower boundary between the doped and undoped regions. This cross-section clearly shows a single crystalline anatase grain extending through 20 nm of the undoped TiO_2 near the substrate into the Er-doped region. (d) Electron backscatter diffraction (EBSD) phase map of individual grains within the same "20/50/20" film as in (b) and (c). The red regions consist of individual anatase grains, and the smaller and less numerous blue regions are individual rutile grains. The black regions either are amorphous or consist of multiple stacked grains of either phase within the thickness of the 90 nm film.

evaluate the surface morphology, we measured the roughness of the as-grown and annealed "10/10/10" films using AFM, as shown in Figure 1c and d, respectively. The AFM height maps yield surface roughness figures of merit, R_a and R_q, that are very similar for as-grown and annealed samples. This low temperature growth and higher temperature annealing process enable preservation of smooth films, as opposed to higher temperature initial growth that leads to much larger surface roughness, as discussed in Figure S1 of the Supporting Information (SI). Low surface roughness is critical for subsequent fabrication of on-chip nanophotonic structures such as waveguides and high quality factor optical resonators. In addition to the low surface roughness, our deposition process yields uniform thickness of TiO_2 films as measured by spectroscopic ellipsometry, with a thickness uniformity over a 100 mm wafer of <1% as would be expected for ALD produced films (see Figure S2, SI).

As described in the previous section, we aim to tailor the Er doping level across a much broader range by controlling the erbium oxide growth rate. To calibrate the Er concentration, we grew a series of samples by varying the evaporation temperature and pulse time of $Er(thd)_3$ and then analyzed these films using SIMS. These samples needed a thicker doped region for sufficient depth resolution, so we grew a "20/50/20" structure, as illustrated in Figure 2a (left), comprising of a 20 nm nominally undoped TiO_2 buffer layer, a 50 nm Er-doped TiO_2 layer, and a 20 nm undoped TiO_2 capping layer. The $Er(thd)_3$ precursor temperatures, $Er(thd)_3$ pulse length, and the experimentally measured Er concentrations via SIMS are listed in Table 1. The range of doping provided by these

Table 1. Sample Deposition and Er Doping Parameters

No.[a]	T[b] (°C)	Δt[c] (s)	doping[d] (ppm)
1	160	8	39200 ± 15680
2	135	8	2950 ± 885
3	110	8	1.7 ± 0.51
4	110	2	0.59 ± 0.24

[a]The sample number. [b]The Er precursor evaporation temperature. [c]The Er precursor pulse length, same as Δt in Figure 1a. [d]The Er concentration determined via SIMS.

conditions spans from below 1 ppm to a few percent. The uncertainty in the Er concentration is provided by the SIMS vendor (see Methods). Previous research has shown that the $Er(thd)_3$ vapor pressure can be reduced by approximately 10-fold with a corresponding drop of ~25 °C in evaporation temperature above 130 °C.[56] Similarly, in this work, the 10-fold reduction of Er dopants between sample No. 1 and sample No. 2 in Table 1 is the result of dropping the evaporation

https://doi.org/10.1021/acsnano.3c09878
ACS Nano 2024, 18, 9929−9941

temperature from 160 to 135 °C. However, the drop in temperature from 135 to 110 °C dramatically decreased the Er concentration (sample No. 3 in Table 1), where the temperature is out of the reported Er(thd)$_3$ evaporation range. Finally, to get sub-ppm level doping we can decrease the pulse length from 8 to 2 s (sample No. 4). Regardless, the lower Er doping concentrations (<2 ppm) in sample Nos. 3 and 4 are significant because they suggest that Er doping at the level needed for coupling to single ions may be achievable via ALD by reducing the number of ErO_x layers overall.

To better visualize the crystalline morphology of the Er:TiO_2 thin films, we also performed electron microscopy on the doped "20/50/20" films used for SIMS analysis (see Methods). Specifically, high-angle annular dark-field scanning transmission electron microscopy (HAADF-STEM) imaging was used to provide additional atomic number contrast to better visualize the heavier Er dopants within the TiO_2 matrix (i.e., a brighter pixel corresponds to a higher Z number). Using this technique, we can clearly see in Figure 2b the increased brightness of the 50 nm thick doped region in a 2950 ppm Er-doped film (same growth conditions as sample No. 2 of Table 1). A corresponding energy-dispersive X-ray spectroscopy (EDS) elemental map of the same cross-section in Figure 2b is shown in the SI (Figure S3), confirming the presence of Er in the doped region. The as-grown films do not show any regular lattice spacing (see Figure S4 of the SI); however, after the oxygen-annealing process, it is common to see large individual anatase grains that are tens of nanometers in thickness extending from the Si substrate, the crystallinity of which does not appear to be impacted by the onset of the relatively high 2950 ppm Er doping (Figure 2c). The lateral extent of these grains can be visualized with electron backscatter diffraction (EBSD) phase mapping in a scanning electron microscope (SEM) operating at 10 kV (with an effective probe depth of a few tens of nanometers), as shown in Figure 2d. The majority of the 4 μm^2 area consists of anatase grains (49.8%), while also exhibiting a much lower percentage of smaller rutile grains (2.0%). The exact depth of the grains probed via EBSD varies based upon accelerating voltage and interaction with the Si substrate underneath (SI, Figure S5), so it is unclear if the black regions in Figure 2d merely represent stacked anatase grains with different orientations or pockets of amorphous TiO_2. Regardless, it is particularly significant that these anatase grains can extend for hundreds of nanometers laterally, as these grains are larger and, overall, the sample offers higher phase purity than the mixed rutile and anatase grain sizes reported in molecular beam deposited TiO_2 on Si.[26] These results suggest that even though our as-grown thin films are amorphous, the oxygen annealing process can induce large anatase grain coarsening and that these resultant grains might serve as a good local crystal host for erbium ions, all without increasing the top layer surface roughness.

Thin Film PLE Measurements. In order to probe the optical properties of the Er ions within the ALD deposited TiO_2, we performed photoluminescence excitation (PLE) spectroscopy within the telecom C-band on the aforementioned "10/10/10" heterostructures grown on Si substrates, wherein only the central 10 nm layer in the heterostructure contains Er dopants. It is important to point out that for these thinner doped heterostructures, EBSD phase maps suggest that they are dominated by a higher percentage of anatase grains and may extend the full 30 nm thickness of the film (see Figure S5a of the SI). To collect the PLE spectra, the samples were cooled to 3.5 K within a closed-cycle cryostat and excited with a continuously tunable C-band laser using confocal microscopy (details are provided in the Methods). As shown in Figure 3,

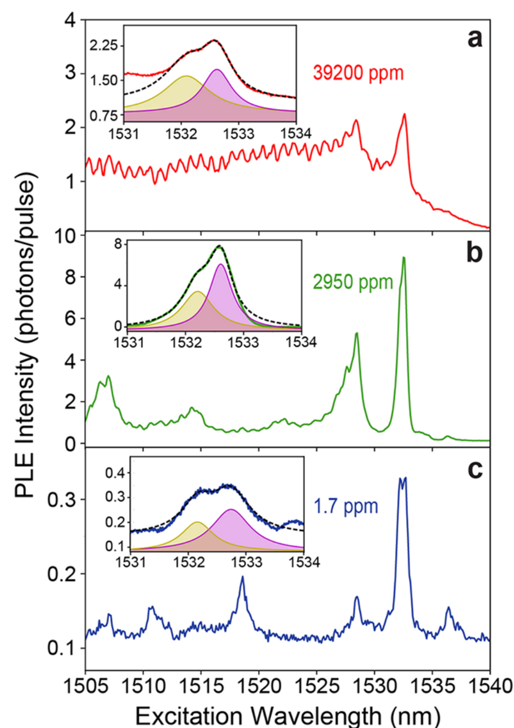

Figure 3. Photoluminescence excitation (PLE) spectra of annealed "10/10/10" Er:TiO_2 thin films. In each of the main panels is a broadband PLE scan from 1505 to 1540 nm, with a scan step size of 0.1 nm. The thin film Er doping levels for the three samples are (a) 39200, (b) 2950, (c) and 1.7 ppm according to Table 1. Insets: corresponding higher resolution PLE scans (step size of 0.01 nm) around the emission peak at 1532.6 nm, giving inhomogeneous line widths of 79.3 ± 2.4, 61.4 ± 1.7, and 102.2 ± 5.4 GHz for the three samples Nos. 1−3, respectively. Each spectrum is fit to a pair of Lorentzian line shapes (black, dashed line), with the resultant individual fits highlighted for clarity (purple and yellow shaded curves).

we measured PLE spectra for oxygen annealed thin films with the three highest doping levels (Table 1): 39200, 2950, and 1.7 ppm. The PLE intensity is the average number of detected photons per 3.5 ms collection window after each 1.5 ms laser pulse. It should be noted that for sample No. 4 at 0.59 ppm, the doping level is too low to be measured because of the long optical excited state lifetime of erbium emission, the thin optically active region, and the finite overall collection efficiency of the setup.

All of the as-grown samples had negligible emission in PLE as a result of the underlying disorder in the films. However, after the 30 min oxygen anneal, all three samples show distinct peaks in the PLE spectra (Figure 3), likely originating from the various crystal field level transitions between the $^4I_{15/2}$ and $^4I_{13/2}$ multiplets within anatase TiO_2.[57] An example of the dramatic increase in PLE brightness for an as-grown versus annealed film is shown in Figure S7 of the SI. Note that the periodic oscillations in the PLE signal are due to Fabry−Perot fringes resulting from partial reflections within the finite thickness of a beamsplitter used in the setup (see SI, Figure S6a). The variation in emission intensities among the three

https://doi.org/10.1021/acsnano.3c09878
ACS Nano 2024, 18, 9929−9941

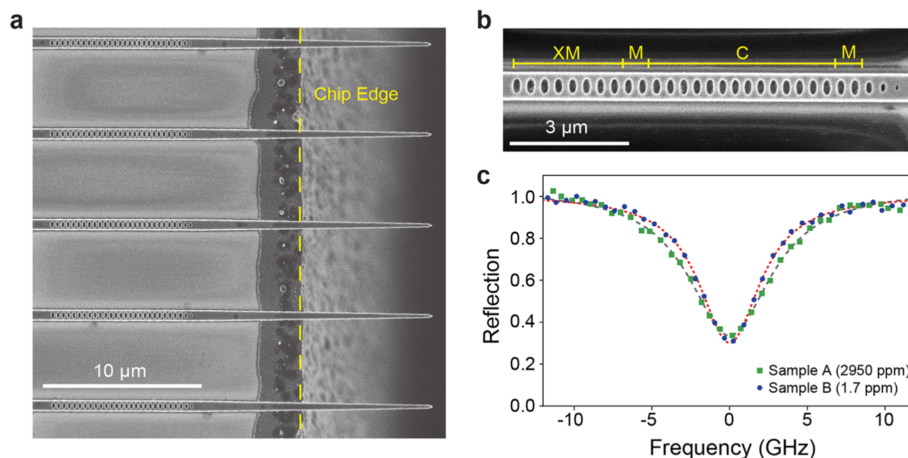

Figure 4. ALD TiO_2−Si photonic crystal cavities. (a) Top view SEM image of fabricated devices from sample B, highlighting the inverse tapered waveguide extending off the edge of the SOI chip (to the right of the yellow dashed line). The dark gray region extending 2−3 μm from the chip edge is due to lateral etching of the original buried oxide layer as part of the undercut process. (b) SEM image highlighting the nanophotonic cavity composed of elliptically shaped holes etched through the TiO_2 and Si device layers. The 14-hole cavity region (denoted by C) consists of a parabolic taper of the lattice constant, there are two mirror holes (M) on each side of the cavity region, and extra mirror holes (XM) are included on the left-hand side of the device because all measurements are performed in a one-sided coupling configuration via the inverse waveguide taper seen in (a). (c) Normalized laser reflection spectra of the photonic cavities from samples A (green squares) and B (blue circles) coupled via a lensed optical fiber at a temperature of 3.5 K. For these reflection scans, the cavities are tuned onto resonance with the Er in anatase TiO_2 transition of interest (λ = 1532.6 nm). Using Lorentzian fits, the cavities from samples A and B have quality factors of $Q = 30220 \pm 890$ (gray, dashed line) and $Q = 40680 \pm 990$ (red, dashed line), respectively.

samples (Figure 3) is mainly attributed to the difference in the doping concentration. In general, higher Er doping typically leads to brighter overall emission; however, as seen by comparing Figure 3a,b, an order of magnitude increase in doping concentration from 2950 to 39200 ppm does not show a commensurate increase in overall brightness for the emission near 1532 nm. Rather, this reduction in brightness is possibly due to ion−ion quenching and cooperative photon up-conversion, which are common at high Er doping concentrations,[58,59] as the estimated ion−ion spacings at 2950 and 39200 ppm are 1.9 and 0.8 nm, respectively. It is also important to note that we have performed PLE measurements on annealed pieces from across a 100 mm growth wafer, and the integrated PLE intensity error is less than the 40% error of the SIMS measurements shown in Table 1.

For each of the three samples, a higher spectral resolution PLE spectrum (0.01 nm step size) near the 1532 nm peak is provided in the inset. Due to the finer spacing, the peak fluorescence varies slightly from that of each corresponding coarse spectrum. Most notable is a pair of closely spaced peaks near 1532.2 and 1532.6 nm, similar to what was observed previously in textured growth of polycrystalline TiO_2.[52] Previous work on Er-doped TiO_2 nanoparticles has experimentally determined the $Y_1 \rightarrow Z_1$ transition to be at 6525 cm^{-1} (1532.57 nm),[57] similar to the predominant peak at 1532.6 nm in our scans. Future temperature-dependent PL and PLE scans are necessary to confirm this level assignment.[39] However, this value differs from the exact energy of the $Y_1 \rightarrow Z_1$ transition reported for epitaxial anatase Er:TiO_2 growth on $LaAlO_3$ at 6518.9 cm^{-1} (1534.00 nm).[40] As shown for a waveguide-based PLE scan (SI, Figure S8), we do not see an obvious peak in this range. This discrepancy could be due to the strain relaxation afforded by the amorphous growth in our polycrystalline anatase films. Fits of these closely spaced peaks enable us to estimate the inhomogeneous line width of the 1532.6 nm transition in each of our three samples (in order of decreasing doping) as 79.3 ± 2.4, 61.4 ± 1.7, and 102.2 ± 5.4 GHz, respectively (Figures 3, insets). The signal-to-noise ratio for the 1.7 ppm sample is poor (Figure 3, inset), as this sample was pumped with ten times higher laser intensity to get sufficiently large detectable signal above background. Therefore, we suspect that this particular transition is power broadened, and waveguide-based PLE measurements at lower power suggest an inhomogeneous line width closer to 44 GHz for the 1.7 ppm sample (see SI, Figure S8). In general, the inhomogeneous line widths of these samples prepared via ALD are broader than epitaxial growth of anatase TiO_2 on $LaAlO_3$ (12.7 GHz for a 4000 ppm film with similar buffer/capping layer thicknesses)[40] and molecular-beam deposited growth of highly textured Er-doped anatase TiO_2 on silicon (11.1 GHz with comparable buffer/capping layer thicknesses and doping).[52] However, it is important to note that they are all much narrower than the previously reported results for Er in ALD-grown Al_2O_3, which show broad emission on the scale of THz.[20,21] Overall, these findings demonstrate the positive impact of the annealing process in promoting the formation of a more ordered lattice structure and enhancing the optical emission characteristics of Er ions in the anatase TiO_2 matrix.

Photonic Crystal Cavity Integration. To demonstrate the potential use of these ALD grown Er:TiO_2 films as a platform for telecom on-chip photonic applications, we integrated the same "10/10/10" thin film heterostructure with silicon photonic crystal cavities based on SOI and measured the resultant Purcell enhancement for ensembles in different doping regimes. For this study, we fabricated devices from two samples with different Er concentrations: Sample A (2950 ppm of Er, deposition condition No. 2 in Table 1) and Sample B (1.7 ppm of Er, No. 3 in Table 1). The waveguide geometry, photonic crystal cavity, and mirror design lattice parameters are identical to that shown previously.[26] In order to compensate for run-to-run etch rate variations, our fabricated devices are designed to have a deliberate elliptical hole size

https://doi.org/10.1021/acsnano.3c09878
ACS Nano 2024, 18, 9929−9941

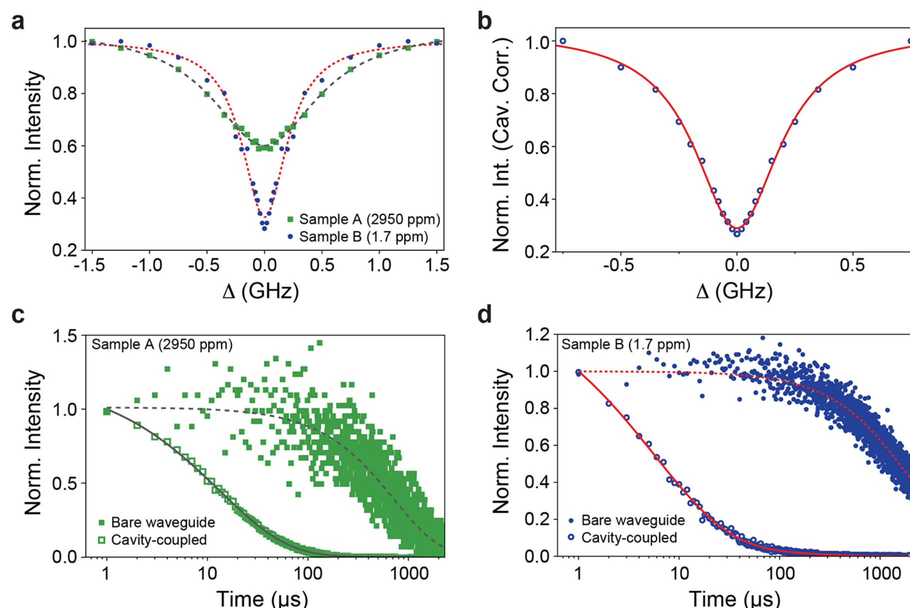

Figure 5. Optical measurements of fabricated devices at T = 3.5 K. (a) Transient spectral hole burning (TSHB) measurement results performed on bare waveguide devices fabricated from sample A (green squares) and sample B (blue circles). The data show the normalized PLE intensity versus the carrier-sideband detuning (Δ) and are symmetric about zero, but they are plotted over the full range for visual clarity. The Lorentzian fits (dashed lines) show a spectral diffusion half-width at half-maximum (HWHM) of 0.56 ± 0.02 GHz for sample A and 0.235 ± 0.012 GHz for sample B. (b) Similar TSHB measurement results for a cavity-coupled Er ensemble on sample B, where the normalized intensity has been corrected to account for the line shape of the same cavity shown in Figure 4c (blue circles). The Lorentzian fit (red, solid line) yields a spectral diffusion line width of 0.223 ± 0.007 GHz. (c) Comparison of the normalized ensemble lifetime of Er ions in a bare waveguide device (green, solid squares) versus the cavity-coupled device (green, open squares) for sample A (2950 ppm). The bare waveguide lifetime is 725 ± 7 μs and the cavity-enhanced lifetime is 13.19 ± 0.07 μs. (d) Comparison of the normalized ensemble lifetime of Er ions in a bare waveguide device (blue, solid circles) versus the cavity-coupled device (blue, open circles) for sample B (1.7 ppm). The bare waveguide lifetime is 1718 ± 5 μs and the cavity-coupled lifetime is 5.7 ± 0.2 μs. For (c) and (d), the bare waveguide lifetimes are fit to a single exponential, and the cavity-enhanced decay times are fit using a stretched exponential as discussed in the text and Methods.

sweep, and there are resonance wavelengths ranging from 1510−1550 nm on each chip. In this work, the desired cavities are nearly resonant at 1532 nm, and as a result, the holes are slightly smaller than those used in the original experiments at 1520 nm (rutile phase, $Y_1 \rightarrow Z_1$ transition). In order to improve the one-way coupling efficiency of our silicon nanophotonics, we performed a multistep process to fully suspend the inverse taper of the waveguide to better mode match to a lensed optical fiber. The substrate and fabrication details are discussed in Methods. To mitigate any potential detrimental defects introduced by the nanophotonic fabrication, we also oxygen annealed the chips at 400 °C after full device fabrication. SEM images of the final devices are shown in Figure 4a,b.

Following the fabrication process, the devices were placed inside a closed-cycle cryostat with a base temperature of 3.5 K for optical characterization using a lensed optical fiber mounted on a three-axis nanopositioner (see Methods). Devices on each sample are screened for cavity resonances 1−2 nm to the blue of the desired optical transition (λ = 1532.6 nm), after which they are tuned (red-shifted) onto resonance via nitrogen gas condensation. Then, each cavity can be characterized by scanning the laser wavelength across the cavity resonance, with their cavity quality factor calculated from the Lorentzian fit of the reflection spectrum as measured with an amplified photodiode. As shown in Figure 4c, device A shows a quality factor of Q = 30220 ± 890, while device B gives Q = 40680 ± 990. Overall, the samples etched from sample A (2950 ppm) had a Q lower than that from sample B (1.7 ppm) by 30−40%, regardless of detuning from the 1532 nm transition, so this is not due to increased absorption from a higher Er concentration. Rather this uniform discrepancy in Q between the two samples is most likely due to the fact that a more complete ErO_x layer (in the case of sample A) hinders the Cl_2 reactive ion etching (RIE) step in the doped region of the TiO_2 film, leading to more hardmask erosion during the RIE process and a subsequently lower etch selectivity. Overall, the quality factors of the cavities are comparable to devices fabricated using thinner (≈22 nm) molecular beam deposited TiO_2 layer with 35 ppm Er doping.[26]

The homogeneous line width of an optical transition is important for many photonics applications and, in particular, for optically addressing single ion quantum memories. A measurement of the homogeneous line widths of individual emitters would provide the best characterization of disorder within each ion's local environment. However, that measurement is not possible for the high doping concentrations, where single emitters cannot be spectrally isolated. Instead, one can perform transient spectral hole burning (TSHB) by sweeping the detuning of two symmetric sideband tones (generated via an electro-optic phase modulator) from the laser carrier frequency to measure the degree of spectral diffusion, which establishes an upper bound on the homogeneous line width.[60] We performed control TSHB measurements via Er embedded in TiO_2 on top of a bare waveguide (no holes). We use 1 ms resonant laser pulses and detect the integrated fluorescence, in a 3.95 ms collection window after the end of the pulse, as a function of the sideband-carrier detuning frequency (Δ). In

Figure 5a, the TSHB results are shown for samples A (green squares) and B (blue circles) with the emitters on bare waveguide devices. The half-width at half-maximum (HWHM) line widths are 0.56 ± 0.02 and 0.235 ± 0.012 GHz, respectively. The higher doped sample A reveals a line width that is broader than sample B by a factor of 2, presumably as a result of the stronger ion−ion interactions. However, for both samples A and B, the spectral diffusion line widths are much narrower than the cavity line widths, which are 6.47 ± 0.19 and 4.80 ± 0.11 GHz for samples A and B, respectively. Thus for both samples, coupling between the emitter and cavity lies in the "bad cavity" regime, where the Purcell enhancement of the optical decay rate scales as Q/V, where Q is the quality factor and V is the mode volume.

We also performed a TSHB measurement on a cavity-coupled Er ensemble for sample B (Figure 5b) when the cavity is resonant with the transition at 1532.6 nm. For this measurement, the continuous-wave (CW) laser power is increased 28-fold while the laser pulse lengths are shortened to 2 μs, specifically to address the sub-ensemble of ions that are well-coupled to the cavity. Finally, the normalized intensity as a function of Δ has been corrected to account for the line shape of the cavity (shown in Figure 4c, blue circles), which modifies the sideband-carrier detuning intensity dependence. In this case, the Lorentzian fit (solid line) yields a spectral diffusion line width of 0.223 ± 0.007 GHz, which is comparable to the TSHB line width for sample B (0.235 ± 0.012 GHz) in Figure 5a. Both the bare and cavity-coupled spectral diffusion line widths are comparable to the narrowest value (0.18 GHz) measured previously for molecular beam deposited thin films with thicker buffer layers,[52] suggesting that the quality of the ALD films as a host for Er are comparable to those grown via molecular beam deposition.

The Purcell enhancement of cavity-coupled ions is an increase in the spontaneous emission rate of the emitter due to coupling with the cavity mode. It is a key parameter for enhancing the light-matter interaction in quantum and optoelectronic devices. To characterize the Purcell enhancement introduced from the nanophotonic cavities for both sample A (2950 ppm) and sample B (1.7 ppm), we performed measurements of the Er emission lifetime using resonant laser pulse excitation. The baseline (non-cavity-coupled) optical lifetime was measured from the same bare control waveguide devices as the TSHB measurements, as illustrated by the closed squares (circles) in green (blue) in Figure 5c (d) for sample A (B). Using a single exponential fit, we found that the natural emission lifetime for the ions on the bare waveguide was approximately 725 μs for sample A and 1718 μs for sample B. An optical lifetime of 1.7 ms for sample B is consistent with what is measured in ALD and molecular beam deposited thin films at sub-100 ppm doping levels, suggesting that even after patterning the reannealed sample does not seem to show signatures of excessive fabrication-induced nonradiative decay. We speculate that the reduced Er optical lifetime seen in sample A is likely due to ion−ion quenching at higher concentration that serves as a nonradiative pathway.[61]

We measured the Purcell-enhanced decay rate (open markers) for each sample using the same cavities in Figure 4c when each cavity is resonant with the Er optical transition at 1532.6 nm. In contrast to the single exponential character of the decay from bare waveguides, the ensembles coupled to each of the cavities show a stretched exponential character (as has been seen previously[26,62]). This is due to the varying coupling strength of ions in the ensemble to the cavity at different spatial positions along the cavity and dipole orientation, with respect to the TE-like fundamental mode. The time constant for the stretched exponential enhanced lifetime for ions coupled to the resonant cavity was 13.19 ± 0.07 μs for sample A and 5.7 ± 0.2 μs for sample B, indicating that the best coupled ions in the ensemble have a Purcell factor of 55 ± 0.6 and 301 ± 11, respectively. Overall, we can see that the Purcell factor for sample A is about 6 times lower than sample B, and the primary culprits are the reduction in the baseline lifetime (725 μs versus 1718 μs) and the modest reduction in cavity Q (3.02×10^4 versus 4.07×10^4). However, this does not fully account for the difference in the cavity-enhanced decay. Because the Purcell factor measured here comes from an ensemble of ions coupled to the cavity, with ions positioned near the cavity nodes being more weakly coupled, the measured stretched exponential decay time provides a lower bound on the lifetime for only the most strongly coupled ions. As a result, it is feasible that the thousand-fold higher concentration of ions in sample A results in more averaging of the ensemble Purcell factor and hence dilutes the contributions of the best coupled ions to yield a lower enhancement. Overall the Purcell factor measured for device B is approximately 50% higher than previously fabricated devices from Er-doped (35 ppm) molecular beam deposited TiO_2 (rutile phase) even though the cavity quality factors were similar.[26] Likely this is due to the aforementioned averaging from the higher doping concentration.

CONCLUSION AND OUTLOOK

Our study showcases a reliable and substrate independent method for growing Er-doped TiO_2 using ALD. One of the most significant findings is the ability to dope these films with Er ions over a large range by controlling the Er dopant precursor temperature and pulse length. This is a level of doping control not usually provided by ALD and can be employed for applications at both ends of the doping spectrum (few percent to sub-ppm). Over the demonstrated doping range, our ALD process offers potential advantages over other methods, such as molecular beam deposition of doped films and implantation of erbium ions in undoped films, in terms of translation to industry because of lower cost and increased scalability. Our characterization of the material proprieties after post-growth oxygen annealing revealed the films to be Er-doped anatase phase TiO_2 with a smooth surface, which can be maintained even after the formation of polycrystalline grains that are hundreds of nanometers wide. Furthermore, our optical measurements revealed distinct optical transitions and a substantially narrower homogeneous line width upper bound for the characteristic emission peaks around 1532 nm for the annealed films. Additionally, the films with low Er concentration exhibited a natural optical lifetime greater than 1 ms, typical of Er in anatase TiO_2. These results suggest that Er:TiO_2 thin films grown by using ALD are a promising material platform for on-chip quantum memory applications. It is particularly important to note that this critical 400 °C oxygen annealing process is CMOS-compatible,[63] further ensuring industrial scalability. A future area of exploration is the possibility of longer annealing times to further increase the anatase grain size or higher annealing temperatures to explore the transition to rutile grains.

Also significant was our coupling of these ALD-grown Er-doped TiO_2 thin films with moderately high quality factor 1D

https://doi.org/10.1021/acsnano.3c09878
ACS Nano 2024, 18, 9929−9941

Si photonic crystal cavities that are enabled, in part, because of the low surface roughness after annealing. The resultant Purcell enhancement demonstrates a significant improvement in the spontaneous emission rate of the Er ions due to the evanescent coupling with the fundamental nanophotonic cavity mode. This enhancement plays a crucial role in achieving more efficient and controlled light-matter interactions. In particular, the low-doped sample exhibited a much higher Purcell enhancement in excess of 300, further confirming the potential of these Er:TiO_2 thin films integrated with nanophotonic cavities at dilute concentrations suitable for quantum technologies.

In order to use these films to spectrally address single Er ion quantum memories, we need to further decrease the doping level to approximately 100 ppb,[23] depending on the resultant single ion line width. It is possible to approach this single ion regime by further reducing the $Er(thd)_3$ precursor temperature or restricting the doped ErO_x layer to a single cycle, which would give a nearly 20-fold reduction in doping, instead of the "10/10/10" doped heterostructure employed here. In restricting all dopants to a delta-doped single layer, it is possible to increase the buffer and capping layer thicknesses to improve the inhomogeneous and spectral diffusion line widths without needing a thick TiO_2 layer that would inevitably lead to challenges in cavity fabrication and reduced evanescent coupling of ions to the cavity. Finally, the smooth film surface enabled by the low temperature growth and anneal can enable facile integration with high quality factor resonators. Particularly interesting is the prospect that the 120 °C ALD growth process can be performed as a lift-off process with conventional polymer resist windows for even more scalable fabrication processes, rather than top-down etching through the thin films that can potentially damage Er qubits. Therefore, this work highlights not only that ALD is a promising technique for quantum device fabrication and integration but also that it could be beneficial for broader Er-based photonics applications, such as on-chip lasing and amplifiers.

METHODS

Er-Doped TiO_2 Thin Film ALD Growth. In this study, we used a Fiji G2 plasma-enhanced ALD system, which can be operated with and without plasma, to produce Er-doped TiO_2 thin films. The deposition process involved the use of titanium isopropoxide (TTIP; from Sigma-Aldrich with 5 N purity), heated to 68 °C, and water (H_2O), maintained at ambient conditions, as precursors for the thermal deposition of TiO_2. During the TiO_2 deposition, the Ar flow was set to 110 sccm to purge out the byproduct and excessive precursors from the chamber. For the Er doping, the tris(2,2,6,6-tetramethyl-3,5-heptanedionato)erbium ($Er(thd)_3$) is from Strem Chemicals with 3 N purity, and it can react via an oxygen plasma to form atomic layers of erbium oxides. The operating power of the oxygen plasma was 300 W with an O_2 flow of 25 sccm and Ar flow of 55 sccm. Unless noted otherwise, all of the thin films are deposited on lightly boron-doped standard silicon substrates from NOVA Electronic Materials and Silicon Valley Microelectronics. The SIMS measurements were performed by Eurofins EAG Laboratories. The relatively large errors of 40% in the individual doping levels within Table 1 are provided by EAG as a result of uncertainty from the Er in TiO_2 calibration process using a thick polycrystalline sample that had been ion implanted at a series of depths using a mass-selective ion source, as well as modest uncertainties in the implantation dose and sample density. The as-grown thin film thicknesses are routinely characterized by X-ray reflection (XRR), which is used to determine the growth rate of TiO_2 and, under these conditions, is estimated to be 0.5−0.6 Å per cycle. The XRD and XRR measurements were completed with a Rigaku SmartLab located at the University of Chicago MRSEC. After the deposition, a thermal anneal was performed at 400 °C for 30 min in a rapid thermal annealing system (Annealsys), with a consistent O_2 flow rate of 500 sccm and resultant pressure near 700 Torr. AFM scans on the as-grown and post-annealed thin films were conducted with a Bruker FastScan system with ScanAsyst.

Electron Microscopy. To prepare samples for scanning transmission electron microscopy (STEM), we used a Zeiss NVision focused ion beam system for specimen "lift-out". Prior to this process, a 2 μm thick carbon layer was deposited on each sample to prevent Ga ion beam damage. A $20 \times 2 \times 5$ μm^3 specimen (length × width × height) was milled from the sample with its height along the (001) direction of the silicon substrate (perpendicular to the wafer surface) and transferred onto a STEM grid with an Oxford Instruments OmniProbe. Following the lift-out procedure, each specimen was thinned further via FIB milling to 100 nm. Finally, each specimen was double-sided-polished in a Gatan PIPS II precision ion polishing system with 0.3 kV Ar^+ to remove any amorphous residue left by the FIB milling process. The polished specimens were then loaded into a Thermofisher Spectra 200 aberration corrected STEM to obtain atomic resolution images of the "20/50/20" Er-doped TiO_2 thin films. The images were taken with an accelerating voltage of 200 kV, yielding a typical resolution of approximately 70 pm. To enhance the contrast of Er atoms, a collection angle larger than 75 mrad is used for HAADF-STEM imaging. The EBSD grain mapping was performed with a JEOL JSM-IT800 SEM with a backscattering electron detector with the probe current fixed at 4.7 nA for a 10 kV accelerating voltage and 7.1 nA for 20 kV.

Thin-Film PLE Measurements. To characterize the emission properties of the Er ions doped in TiO_2, we probed the Er ion optical properties using photoluminescence excitation (PLE) spectroscopy near 1.5 μm. The samples were cooled to 3.5 K within a Montana s50 Cryostation. The measurement configuration consisted of a Toptica CTL 1500 tunable laser passed through a pair of fiber-coupled acousto-optic modulators (MT80-IIR30-Fio-PM0.5-J1-A-Ic2, AA Opto Electronic) and then coupled into a fixed focus free space collimator. A 50:50 plate beamsplitter separates excitation and collection paths, with the excitation path collimating light into a 0.65 NA objective lens focused on the thin film sample using a 3-axis periscope stage (Newport). Emitted photons (fluorescence) are routed back through the beamsplitter into the collection pathway, which consists of two long-pass filters (FELH1500, Thorlabs) and a second fiber-to-free-space collimator, with a single-mode fiber going to the detector. Single telecom photons were detected via a superconducting nanowire single photon detector (SNSPD) from Quantum Opus within a second cryostat, which was optimized for near-1.5 μm detection at ≈80% quantum efficiency. The collected light is gated by an additional modulator (AMM-55-4-50-1550-2FP, Brimrose) to prevent latching of the SNSPD during laser excitation. Event timing and single photon counting are handled by a dedicated Pulse Streamer 8/2 (Swabian Instruments) and a Time Tagger Ultra (Swabian Instruments), respectively. For each PLE scan, at each wavelength, one measurement shot consisted of an excitation pulse of 1.5 ms followed by a collection interval of 3.5 ms, averaged over 10,000 shots for each wavelength; this generates a histogram of the single photon counts detected during the collection window. The overall intensity of the collected signal is integrated for each wavelength to produce a PLE spectrum. A diagram of the thin-film PLE measurement configuration is presented in Figure S6a of the SI.

Nanophotonic Device Fabrication. The silicon-on-insulator wafers used for nanocavity fabrication have a 220 nm thick Si device layer and 2 μm thick buried oxide (Soitec). The device layer is lightly boron-doped with a resistivity of 10 Ω·cm. Following ALD thin film growth, all fabrication is performed in the Center for Nanoscale Materials cleanroom at Argonne National Laboratory and is similar to the process flow outlined in the Supporting Information of prior work.[26] As part of a later step in the device fabrication process flow, we need to strip the SiO_2 hardmask in a buffered oxide etch (BOE), so prior to the SiO_2 hardmask deposition, we perform a 30 min

https://doi.org/10.1021/acsnano.3c09878
ACS Nano 2024, 18, 9929−9941

oxygen anneal (Annealsys) at 400 °C in pure oxygen, which makes the Er:TiO_2 film highly resistant to later BOE exposure. We use standard electron beam lithography (JEOL 8100) with a ZEP 520A resist on top of a hardmask of SiO_2 deposited via plasma enhanced chemical vapor deposition (PECVD, Oxford PlasmaLab 100). Fluorine-based etching is used for mask transfer to the SiO_2, Cl_2 is used to etch through the TiO_2 layer, and HBr/O_2 is used to etch through the Si device layer. All etching is performed in an Oxford PlasmaLab 100 inductively coupled plasma (ICP) RIE system. As mentioned in the main text, the etch rate of Er-doped TiO_2 decreases with increasing doping concentration. A thick reference sample of commensurate doping is used to calibrate the Cl_2 etch rate of TiO_2 for the different doping concentrations. Unlike the waveguide geometry employed previously,[26] the inverse tapered waveguides are fixed length, designed to be truncated, masked, and vapor etched for better coupling between the on-chip waveguide and the lensed fiber. The full details of the taper design, hardmask chemistry, undercut process, and fiber-to-waveguide coupling efficiency estimates are presented elsewhere.[64] Within our large array of devices, there are clusters of nominally identically designed cavities with the same hole size (the hole size is swept to account for run-to-run variations in the TiO_2 and Si etch rates). The ideal device resonances are approximately 1541−1543 nm at room temperature to account for the 12 nm resonance blueshift when cooled to 3.5 K. Experimentally, the cavity *Q*s at room temperature are within about 10% of each other for a particular etching run/sample, and each resonance is typically within ∼2 nm of the other devices within the cluster.

Device Measurements. We measured the photonic crystal cavity devices in a separate Montana Instruments s100 Cryostation with a sample base temperature of 3.5 K. The nanopositioner, lensed fiber configuration, nitrogen gas tuning, optical modulators, optical fiber network, and single photon detectors are nearly identical to work published previously.[26] The schematic of the optical measurement setup for nanocavities can be seen in Figure S6b of the SI. For both the TSHB and lifetime control measurements (Figure 5a,c,d), we used bare waveguide devices fabricated on the same chip as the cavity devices. For these control measurements, one shot consisted of a 1 ms laser pulse length and 3.95 ms photon collection interval, during which the single photon counts were detected via a SNSPD in a separate cryostat. For the TSHB control measurements the total number of detected photons was integrated for each sideband detuning frequency (Δ) output with a function generator to the phase modulator. For the bare waveguide lifetime control measurements (Figure 5c,d, solid markers), there was no sideband tone, and the lifetime is fit to a single exponential of the single photon detection times (via a qutools quTAG time tagger) after accounting for the SNSPD dark count rate (30 Hz). For the cavity-coupled TSHB measurement (Figure 5b), the input CW laser power was increased by 28× but the laser pulse lengths were shortened to 2 μs to probe spectral diffusion for the ions that are well-coupled to the cavity and will have cavity-enhanced decay rates. The normalized intensity as a function of Δ (Figure 5b) has been corrected to account for the Lorentzian line shape of the cavity (full-width at half-maximum, FWHM = 4.8 GHz); shown in Figure 4c, green dots), which modifies the intensity dependence on sideband-carrier laser detuning. Similar to the cavity-coupled TSHB measurements, the cavity-enhanced lifetime (Purcell) measurements are performed using 2 μs resonant laser pulses but with no driven sideband tone. For all device measurements, there is a 2 μs delay between the end of the incident laser pulse and the opening of the collection path intensity modulator to the superconducting nanowire single photon detector. For the cavity-coupled TSHB and lifetime measurements, the cavity resonance is systematically red-shifted onto the optical resonance at 1532.6 nm using nitrogen gas ice condensation, while periodically monitoring the spectral position of the cavity via a CW laser reflection scan. For the cavity-coupled lifetime measurements shown in Figure 5c,d (open markers), the solid line fits are in the form of a fast-decay stretched exponential and a slow single exponential, as described in detail in the SI of previous work,[26] where we use a nonlinear model fit to find the stretched exponential time constant (τ_{fast}) and interpret 1/τ_{fast} as the fastest Purcell-enhanced lifetime of the ensemble.

ASSOCIATED CONTENT

Supporting Information

The Supporting Information is available free of charge at https://pubs.acs.org/doi/10.1021/acsnano.3c09878.

Additional experimental and analysis details, such as the AFM scan of an ALD TiO_2 film grown at 300 °C, TiO_2 deposition uniformity, STEM EDS elemental mapping of the doped "20/50/20" heterostructure, comparison of crystallinity of Er-doped TiO_2 pre- and post-400 °C oxygen annealing, EBSD phase maps for thinner "10/10/10" TiO_2 films used for optical measurements, experimental configurations used for optical measurements, PLE results from as-grown samples, and PLE measurements on a 1.7 ppm waveguide-based device (PDF)

AUTHOR INFORMATION

Corresponding Authors

Supratik Guha − *Pritzker School of Molecular Engineering, University of Chicago, Chicago, Illinois 60637, United States; Materials Science Division, Argonne National Laboratory, Lemont, Illinois 60439, United States; Center for Molecular Engineering, Argonne National Laboratory, Lemont, Illinois 60439, United States;* orcid.org/0000-0001-5071-8318; Email: sguha@anl.gov

Alan M. Dibos − *Center for Molecular Engineering, Center for Nanoscale Materials, and Nanoscience and Technology Division, Argonne National Laboratory, Lemont, Illinois 60439, United States;* orcid.org/0000-0001-5935-1364; Email: adibos@anl.gov

Authors

Cheng Ji − *Pritzker School of Molecular Engineering, University of Chicago, Chicago, Illinois 60637, United States; Materials Science Division, Argonne National Laboratory, Lemont, Illinois 60439, United States*

Michael T. Solomon − *Pritzker School of Molecular Engineering, University of Chicago, Chicago, Illinois 60637, United States; Materials Science Division, Argonne National Laboratory, Lemont, Illinois 60439, United States; Center for Molecular Engineering, Argonne National Laboratory, Lemont, Illinois 60439, United States;* orcid.org/0000-0002-2716-668X

Gregory D. Grant − *Pritzker School of Molecular Engineering, University of Chicago, Chicago, Illinois 60637, United States; Materials Science Division, Argonne National Laboratory, Lemont, Illinois 60439, United States;* orcid.org/0000-0002-6843-5938

Koichi Tanaka − *Pritzker School of Molecular Engineering, University of Chicago, Chicago, Illinois 60637, United States;* orcid.org/0000-0002-3180-7881

Muchuan Hua − *Center for Nanoscale Materials, Argonne National Laboratory, Lemont, Illinois 60439, United States*

Jianguo Wen − *Center for Nanoscale Materials, Argonne National Laboratory, Lemont, Illinois 60439, United States;* orcid.org/0000-0002-3755-0044

Sagar Kumar Seth − *Pritzker School of Molecular Engineering, University of Chicago, Chicago, Illinois 60637, United States; Materials Science Division, Argonne National Laboratory, Lemont, Illinois 60439, United States*

https://doi.org/10.1021/acsnano.3c09878
ACS Nano 2024, 18, 9929−9941

Connor P. Horn − *Pritzker School of Molecular Engineering, University of Chicago, Chicago, Illinois 60637, United States; Materials Science Division, Argonne National Laboratory, Lemont, Illinois 60439, United States;* orcid.org/0000-0002-8385-4882

Ignas Masiulionis − *Pritzker School of Molecular Engineering, University of Chicago, Chicago, Illinois 60637, United States; Materials Science Division, Argonne National Laboratory, Lemont, Illinois 60439, United States*

Manish Kumar Singh − *Pritzker School of Molecular Engineering, University of Chicago, Chicago, Illinois 60637, United States;* Present Address: memQ Inc., Chicago, IL 60615, United States; orcid.org/0000-0002-2193-2689

Sean E. Sullivan − *Materials Science Division, Argonne National Laboratory, Lemont, Illinois 60439, United States; Center for Molecular Engineering, Argonne National Laboratory, Lemont, Illinois 60439, United States;* Present Address: memQ Inc., Chicago, IL 60615, United States; orcid.org/0000-0002-5217-1069

F. Joseph Heremans − *Materials Science Division, Argonne National Laboratory, Lemont, Illinois 60439, United States; Center for Molecular Engineering, Argonne National Laboratory, Lemont, Illinois 60439, United States; Pritzker School of Molecular Engineering, University of Chicago, Chicago, Illinois 60637, United States;* orcid.org/0000-0003-3337-7958

David D. Awschalom − *Pritzker School of Molecular Engineering, University of Chicago, Chicago, Illinois 60637, United States; Materials Science Division, Argonne National Laboratory, Lemont, Illinois 60439, United States; Center for Molecular Engineering, Argonne National Laboratory, Lemont, Illinois 60439, United States; Department of Physics, University of Chicago, Chicago, Illinois 60637, United States;* orcid.org/0000-0002-8591-2687

Complete contact information is available at:
https://pubs.acs.org/10.1021/acsnano.3c09878

Notes

The authors declare no competing financial interest.

ACKNOWLEDGMENTS

The authors would like to thank D. Czaplewski, C. S. Miller, and R. Divan for assistance with device fabrication. The authors acknowledge the Q-NEXT Quantum Center, a U.S. Department of Energy, Office of Science, National Quantum Information Science Research Center, under Award Number DE-FOA-0002253 for support (C.J., G.D.G., C.P.H., I.M., S.K.S, D.D.A., S.G., and A.M.D.). AFM characterization, oxygen annealing, electron microscopy, and cavity device fabrication were performed at the Center for Nanoscale Materials, a U.S. Department of Energy Office of Science User Facility, supported by the U.S. DOE, Office of Basic Energy Sciences, under Contract No. DE-AC02-06CH11357. Additional support (M.H. and J.W.) for TEM characterization is supported by Quantum Information Science research funding from the U.S. DOE, Office of Science User Facility. Additional materials characterization support (M.T.S., S.E.S., and F.J.H.) was provided by the U.S. Department of Energy, Office of Science; Basic Energy Sciences, Materials Sciences, and Engineering Division. Additional support (M.K.S.) for growth capabilities was provided by the Center for Novel Pathways to Quantum Coherence in Materials, an Energy Frontier Research Center funded by the U.S. Department of Energy, Office of Science, Basic Energy Sciences under Award No. DE-AC02-05CH11231.

REFERENCES

(1) Wehner, S.; Elkouss, D.; Hanson, R. Quantum Internet: A Vision for the Road Ahead. *Science* **2018**, *362*, eaam9288.

(2) Briegel, H.-J.; Dür, W.; Cirac, J. I.; Zoller, P. Quantum Repeaters: The Role of Imperfect Local Operations in Quantum Communication. *Phys. Rev. Lett.* **1998**, *81*, 5932−5935.

(3) Lvovsky, A. I.; Sanders, B. C.; Tittel, W. Optical Quantum Memory. *Nat. Photonics* **2009**, *3*, 706−714.

(4) Sangouard, N.; Simon, C.; de Riedmatten, H.; Gisin, N. Quantum Repeaters Based on Atomic Ensembles and Linear Optics. *Rev. Mod. Phys.* **2011**, *83*, 33−80.

(5) Singh, M. K.; Jiang, L.; Awschalom, D.; Guha, S. Key Device and Materials Specifications for a Repeater Enabled Quantum Internet. *IEEE Trans. Quantum Eng.* **2021**, *2*, 1−9.

(6) Böttger, T.; Thiel, C. W.; Cone, R. L.; Sun, Y. Effects of Magnetic Field Orientation on Optical Decoherence in Er^{3+}:Y_2SiO_5. *Phys. Rev. B* **2009**, *79*, 115104.

(7) Serrano, D.; Kuppusamy, S. K.; Heinrich, B.; Fuhr, O.; Hunger, D.; Ruben, M.; Goldner, P. Ultra-Narrow Optical Linewidths in Rare-Earth Molecular Crystals. *Nature* **2022**, *603*, 241−246.

(8) Zhong, M.; Hedges, M. P.; Ahlefeldt, R. L.; Bartholomew, J. G.; Beavan, S. E.; Wittig, S. M.; Longdell, J. J.; Sellars, M. J. Optically Addressable Nuclear Spins in a Solid with a Six-Hour Coherence Time. *Nature* **2015**, *517*, 177−180.

(9) Wang, Y.; Um, M.; Zhang, J.; An, S.; Lyu, M.; Zhang, J.-N.; Duan, L. M.; Yum, D.; Kim, K. Single-Qubit Quantum Memory Exceeding Ten-Minute Coherence Time. *Nat. Photonics* **2017**, *11*, 646−650.

(10) Rančić, M.; Hedges, M. P.; Ahlefeldt, R. L.; Sellars, M. J. Coherence Time of over a Second in a Telecom-Compatible Quantum Memory Storage Material. *Nat. Phys.* **2018**, *14*, 50−54.

(11) Raha, M.; Chen, S.; Phenicie, C. M.; Ourari, S.; Dibos, A. M.; Thompson, J. D. Optical Quantum Nondemolition Measurement of a Single Rare Earth Ion Qubit. *Nat. Commun.* **2020**, *11*, 1605.

(12) Chen, S.; Raha, M.; Phenicie, C. M.; Ourari, S.; Thompson, J. D. Parallel Single-Shot Measurement and Coherent Control of Solid-State Spins Below the Diffraction Limit. *Science* **2020**, *370*, 592−595.

(13) Le Dantec, M.; Rančić, M.; Lin, S.; Billaud, E.; Ranjan, V.; Flanigan, D.; Bertaina, S.; Chaneliere, T.; Goldner, P.; Erb, A.; Liu, R. B.; Esteve, D.; Vion, D.; Flurin, E.; Bertet, P. Twenty-Three-Millisecond Electron Spin Coherence of Erbium Ions in a Natural-Abundance Crystal. *Sci. Adv.* **2021**, *7*, na DOI: 10.1126/sciadv.abj9786.

(14) Barnett, P. S.; Longdell, J. J. Theory of Microwave-Optical Conversion Using Rare-Earth-Ion Dopants. *Phys. Rev. A* **2020**, *102*, 063718.

(15) Xie, T.; Rochman, J.; Bartholomew, J. G.; Ruskuc, A.; Kindem, J. M.; Craiciu, I.; Thiel, C. W.; Cone, R. L.; Faraon, A. Characterization of Er^{3+}:YVO_4 for Microwave to Optical Transduction. *Phys. Rev. B* **2021**, *104*, 054111.

(16) Rochman, J.; Xie, T.; Bartholomew, J. G.; Schwab, K. C.; Faraon, A. Microwave-to-Optical Transduction with Erbium Ions Coupled to Planar Photonic and Superconducting Resonators. *Nat. Commun.* **2023**, *14*, 1−9.

(17) Wang, B.; Zhou, P.; Wang, X. Recent Progress in On-Chip Erbium-Based Light Sources. *Appl. Sci.* **2022**, *12*, 11712.

(18) Xin, M.; Li, N.; Singh, N.; Ruocco, A.; Su, Z.; Magden, E. S.; Notaros, J.; Vermeulen, D.; Ippen, E. P.; Watts, M. R.; Kärtner, F. X. Optical Frequency Synthesizer with an Integrated Erbium Tunable Laser. *Light: Sci. Appl.* **2019**, *8*, 122.

(19) Li, T.; Wu, K.; Cai, M.; Xiao, Z.; Zhang, H.; Li, C.; Xiang, J.; Huang, Y.; Chen, J. A Single-Frequency Single-Resonator Laser on Erbium-Doped Lithium Niobate on Insulator. *APL Photonics* **2021**, *6*, 101301.

(20) Rönn, J.; Karvonen, L.; Kauppinen, C.; Perros, A. P.; Peyghambarian, N.; Lipsanen, H.; Säynätjoki, A.; Sun, Z. Atomic Layer Engineering of Er-Ion Distribution in Highly Doped Er:Al_2O_3 for Photoluminescence Enhancement. *ACS Photonics* **2016**, *3*, 2040−2048.
(21) Rönn, J.; Zhang, W.; Autere, A.; Leroux, X.; Pakarinen, L.; Alonso-Ramos, C.; Säynätjoki, A.; Lipsanen, H.; Vivien, L.; Cassan, E.; Sun, Z. Ultra-High On-Chip Optical Gain in Erbium-Based Hybrid Slot Waveguides. *Nat. Commun.* **2019**, *10*, 432.
(22) Chen, Z.; Wan, L.; Gao, S.; Zhu, K.; Zhang, M.; Li, Y.; Huang, X.; Li, Z. On-Chip Waveguide Amplifiers for Multi-Band Optical Communications: A Review and Challenge. *J. Lightwave Technol.* **2022**, *40*, 3364−3373.
(23) Dibos, A. M.; Raha, M.; Phenicie, C. M.; Thompson, J. D. Atomic Source of Single Photons in the Telecom Band. *Phys. Rev. Lett.* **2018**, *120*, 243601.
(24) Uysal, M. T.; Raha, M.; Chen, S.; Phenicie, C. M.; Ourari, S.; Wang, M.; Van de Walle, C. G.; Dobrovitski, V. V.; Thompson, J. D. Coherent Control of a Nuclear Spin via Interactions with a Rare-Earth Ion in the Solid State. *PRX Quantum* **2023**, *4*, 010323.
(25) Ourari, S.; Dusanowski, Ł.; Horvath, S. P.; Uysal, M. T.; Phenicie, C. M.; Stevenson, P.; Raha, M.; Chen, S.; Cava, R. J.; de Leon, N. P.; Thompson, J. D. Indistinguishable Telecom Band Photons from a Single Er Ion in the Solid State. *Nature* **2023**, *620*, 977−981.
(26) Dibos, A. M.; Solomon, M. T.; Sullivan, S. E.; Singh, M. K.; Sautter, K. E.; Horn, C. P.; Grant, G. D.; Lin, Y.; Wen, J.; Heremans, F. J.; Guha, S.; Awschalom, D. D. Purcell Enhancement of Erbium Ions in TiO_2 on Silicon Nanocavities. *Nano Lett.* **2022**, *22*, 6530−6536.
(27) Gritsch, A.; Weiss, L.; Früh, J.; Rinner, S.; Reiserer, A. Narrow Optical Transitions in Erbium-Implanted Silicon Waveguides. *Phys. Rev. X* **2022**, *12*, 041009.
(28) Gritsch, A.; Ulanowski, A.; Reiserer, A. Purcell Enhancement of Single-Photon Emitters in Silicon. *Optica* **2023**, *10*, 783.
(29) Kumar, P.; Lynch, J.; Song, B.; Ling, H.; Barrera, F.; Kisslinger, K.; Zhang, H.; Anantharaman, S. B.; Digani, J.; Zhu, H.; Choudhury, T. H.; McAleese, C.; Wang, X.; Conran, B. R.; Whear, O.; Motala, M. J.; Snure, M.; Muratore, C.; Redwing, J. M.; Glavin, N. R.; et al. Light−Matter Coupling in Large-Area van Der Waals Superlattices. *Nat. Nanotechnol.* **2022**, *17*, 182−189.
(30) López-Morales, G. I.; Li, M.; Hampel, A.; Satapathy, S.; Proscia, N. V.; Jayakumar, H.; Lozovoi, A.; Pagliero, D.; Lopez, G. E.; Menon, V. M.; Flick, J.; Meriles, C. A. Investigation of Photon Emitters in Ce-Implanted Hexagonal Boron Nitride. *Opt. Mater. Express* **2021**, *11*, 3478−3485.
(31) Biyikli, N.; Haider, A. Atomic Layer Deposition: An Enabling Technology for the Growth of Functional Nanoscale Semiconductors. *Semicond. Sci. Technol.* **2017**, *32*, 093002.
(32) Shahin, D. I.; Tadjer, M. J.; Wheeler, V. D.; Koehler, A. D.; Anderson, T. J.; Eddy, C. R.; Christou, A. Electrical characterization of ALD HfO2 high-k dielectrics on (201) β-Ga2O3. *Appl. Phys. Lett.* **2018**, *112*, 042107.
(33) Ovanesyan, R. A.; Filatova, E. A.; Elliott, S. D.; Hausmann, D. M.; Smith, D. C.; Agarwal, S. Atomic Layer Deposition of Silicon-Based Dielectrics for Semiconductor Manufacturing: Current Status and Future Outlook. *J. Vac. Sci. Technol.* **2019**, *37*, 060904.
(34) Chakrabarti, B.; Chan, H.; Alam, K.; Koneru, A.; Gage, T. E.; Ocola, L. E.; Divan, R.; Rosenmann, D.; Khanna, A.; Grisafe, B.; Sanders, T.; Datta, S.; Arslan, I.; Sankaranarayan, S. K. R. S.; Guha, S. Nanoporous Dielectric Resistive Memories Using Sequential Infiltration Synthesis. *ACS Nano* **2021**, *15*, 4155−4164.
(35) Zheng, J.; Xue, X.; Ji, C.; Yuan, Y.; Sun, K.; Rosenmann, D.; Wang, L.; Wu, J.; Campbell, J. C.; Guha, S. Dynamic-Quenching of a Single-Photon Avalanche Photodetector Using an Adaptive Resistive Switch. *Nat. Commun.* **2022**, *13*, 1517.
(36) Dette, C.; Pérez-Osorio, M. A.; Kley, C. S.; Punke, P.; Patrick, C. E.; Jacobson, P.; Giustino, F.; Jung, S. J.; Kern, K. TiO_2 Anatase with a Bandgap in the Visible Region. *Nano Lett.* **2014**, *14*, 6533−6538.
(37) Kanai, S.; Heremans, F. J.; Seo, H.; Wolfowicz, G.; Anderson, C. P.; Sullivan, S. E.; Onizhuk, M.; Galli, G.; Awschalom, D. D.; Ohno, H. Generalized Scaling of Spin Qubit Coherence in over 12,000 Host Materials. *Proc. Natl. Acad. Sci. U. S. A.* **2022**, *119*, e2121808119.
(38) Stevenson, P.; Phenicie, C. M.; Gray, I.; Horvath, S. P.; Welinski, S.; Ferrenti, A. M.; Ferrier, A.; Goldner, P.; Das, S.; Ramesh, R.; Cava, R. J.; de Leon, N. P.; Thompson, J. D. Erbium-Implanted Materials for Quantum Communication Applications. *Phys. Rev. B* **2022**, *105*, 224106.
(39) Phenicie, C. M.; Stevenson, P.; Welinski, S.; Rose, B. C.; Asfaw, A. T.; Cava, R. J.; Lyon, S. A.; de Leon, N. P.; Thompson, J. D. Narrow Optical Line Widths in Erbium Implanted in TiO_2. *Nano Lett.* **2019**, *19*, 8928−8933.
(40) Shin, K.; Gray, I.; Marcaud, G.; Horvath, S. P.; Walker, F. J.; Thompson, J. D.; Ahn, C. H. Er-Doped Anatase TiO_2 Thin Films on $LaAlO_3$ (001) for Quantum Interconnects (QuICs). *Appl. Phys. Lett.* **2022**, *121*, 081902.
(41) Ji, C.; Grant, G. D.; Singh, M. K.; Seth, S.; Tanaka, K.; Dibos, A. M.; Guha, S. Optical Properties of Er Ion Doped TiO_2 with Atomic Layer Deposition. *Quantum Information Science, Sensing, and Computation XV* **2023**, 1251702.
(42) Niemelä, J.-P.; Marin, G.; Karppinen, M. Titanium Dioxide Thin Films by Atomic Layer Deposition: A Review. *Semicond. Sci. Technol.* **2017**, *32*, 093005.
(43) Hackler, R. A.; Kang, G.; Schatz, G. C.; Stair, P. C.; Van Duyne, R. P. Analysis of TiO_2 Atomic Layer Deposition Surface Chemistry and Evidence of Propene Oligomerization Using Surface-Enhanced Raman Spectroscopy. *J. Am. Chem. Soc.* **2019**, *141*, 414−422.
(44) O'Donnell, S.; Jose, F.; Shiel, K.; Snelgrove, M.; McFeely, C.; McGill, E.; O'Connor, R. Thermal and Plasma Enhanced Atomic Layer Deposition of Ultrathin TiO_2 on Silicon from Amide and Alkoxide Precursors: Growth Chemistry and Photoelectrochemical Performance. *J. Phys. D: Appl. Phys.* **2022**, *55*, 085105.
(45) Kim, H.; An, J.; Maeng, S.; Shin, J.-S.; Choi, E.; Yun, J.-Y. Decomposition Characteristics of the TTIP (Tetraisopropyl Orthotitanate) Precursor for Atomic Layer Deposition. *Materials* **2022**, *15*, 3021.
(46) Van, T. T.; Bargar, J. R.; Chang, J. P. Er Coordination in Y_2O_3 Thin Films Studied by Extended X-Ray Absorption Fine Structure. *J. Appl. Phys.* **2006**, *100*, 023115.
(47) Hoang, J.; Van, T. T.; Sawkar-Mathur, M.; Hoex, B.; Van de Sanden, M. C. M.; Kessels, W. M. M.; Ostroumov, R.; Wang, K. L.; Bargar, J. R.; Chang, J. P. Optical Properties of Y_2O_3 Thin Films Doped with Spatially Controlled Er^{3+} by Atomic Layer Deposition. *J. Appl. Phys.* **2007**, *101*, 123116.
(48) Van, T. T.; Hoang, J.; Ostroumov, R.; Wang, K. L.; Bargar, J. R.; Lu, J.; Blom, H.-O.; Chang, J. P. Nanostructure And Temperature-Dependent Photoluminescence Of Er-Doped Y_2O_3 Thin Films for Micro-Optoelectronic Integrated Circuits. *J. Appl. Phys.* **2006**, *100*, 073512.
(49) Van, T. T.; Chang, J. P. Controlled Erbium Incorporation and Photoluminescence of Er-Doped Y_2O_3. *Appl. Phys. Lett.* **2005**, *87*, 011907.
(50) Aarik, J.; Aidla, A.; Uustare, T.; Sammelselg, V. Morphology and Structure of TiO_2 Thin Films Grown by Atomic Layer Deposition. *J. Cryst. Growth* **1995**, *148*, 268−275.
(51) Singh, M. K.; Prakash, A.; Wolfowicz, G.; Wen, J.; Huang, Y.; Rajh, T.; Awschalom, D. D.; Zhong, T.; Guha, S. Epitaxial Er-Doped Y_2O_3 on Silicon for Quantum Coherent Devices. *APL Mater.* **2020**, *8*, 031111.
(52) Singh, M. K.; Wolfowicz, G.; Wen, J.; Sullivan, S. E.; Prakash, A.; Dibos, A. M.; Awschalom, D. D.; Heremans, F. J.; Guha, S. Development of a Scalable Quantum Memory Platform − Materials Science of Erbium-Doped TiO_2 Thin Films on Silicon. *arXiv:2202.05376 [cond-mat.mtrl-sci]* **2022**.

https://doi.org/10.1021/acsnano.3c09878
ACS Nano 2024, 18, 9929−9941

(53) Horprathum, M.; Chindaudom, P.; Limnonthakul, P.; Eiamchai, P.; Nuntawong, N.; Patthanasettakul, V.; Pokaipisit, A.; Limsuwan, P. Fabrication and Characterization of Hydrophilic TiO_2 Thin Films on Unheated Substrates Prepared by Pulsed DC Reactive Magnetron Sputtering. *J. Nanomater* **2010**, *2010*, 1.

(54) Zaumseil, P. High-Resolution Characterization of the Forbidden Si 200 and Si 222 Reflections. *J. Appl. Crystallogr.* **2015**, *48*, 528−532.

(55) Niilisk, A.; Moppel, M.; Pärs, M.; Sildos, I.; Jantson, T.; Avarmaa, T.; Jaaniso, R.; Aarik, J. Structural Study of TiO_2 Thin Films by Micro-Raman Spectroscopy. *Open Phys.* **2006**, *4*, 105−116.

(56) Sicre, J. E.; Dubois, J. T.; Eisentraut, K. J.; Sievers, R. E. Volatile Lanthanide Chelates. ii. Vapor Pressures, Heats of Vaporization, and Heats of Sublimation. *J. Am. Chem. Soc.* **1969**, *91*, 3476−3481.

(57) Luo, W.; Fu, C.; Li, R.; Liu, Y.; Zhu, H.; Chen, X. Er^{3+}-Doped Anatase TiO_2 Nanocrystals: Crystal-Field Levels, Excited-State Dynamics, Upconversion, and Defect Luminescence. *Small* **2011**, *7*, 3046−3056.

(58) Hehlen, M. P.; Cockroft, N. J.; Gosnell, T. R.; Bruce, A. J.; Nykolak, G.; Shmulovich, J. Uniform Upconversion in High-Concentration Er^{3+}-Doped Soda Lime Silicate and Aluminosilicate Glasses. *Opt. Lett.* **1997**, *22*, 772−774.

(59) Vonderhaar, A.; Stone, M. P.; Campbell, J.; Hawkins, T. W.; Ballato, J.; Dragic, P. D. Concentration Quenching and Clustering Effects In Er:YAG-Derived All-Glass Optical Fiber. *Opt. Mater. Express* **2021**, *11*, 3587−3599.

(60) Weiss, L.; Gritsch, A.; Merkel, B.; Reiserer, A. Erbium dopants in nanophotonic silicon waveguides. *Optica* **2021**, *8*, 40−41.

(61) Michael, C. P.; Yuen, H. B.; Sabnis, V. A.; Johnson, T. J.; Sewell, R.; Smith, R.; Jamora, A.; Clark, A.; Semans, S.; Atanackovic, P. B.; Painter, O. Growth, Processing, and Optical Properties of Epitaxial Er_2O_3 on Silicon. *Opt. Express* **2008**, *16*, 19649−19666.

(62) Lei, M.; Fukumori, R.; Rochman, J.; Zhu, B.; Endres, M.; Choi, J.; Faraon, A. Many-Body Cavity Quantum Electrodynamics with Driven Inhomogeneous Emitters. *Nature* **2023**, *617*, 271−276.

(63) Sedky, S.; Witvrouw, A.; Bender, H.; Baert, K. Experimental Determination of the Maximum Post-Process Annealing Temperature for Standard CMOS Wafers. *IEEE Trans. Electron Devices* **2001**, *48*, 377−385.

(64) Solomon, M. T.; Koppenhöfer, M.; Ji, C.; Grant, G.; Masiulionis, I.; Sullivan, S. E.; Heremans, F. J.; Guha, S.; Awschalom, D. D.; Clerk, A. A.; Dibos, A. M. Anomalous Purcell Decay of Strongly Driven Inhomogeneous Emitters Coupled to a Cavity. *arXiv:2309.16641 [quant-ph]* **2023**.

https://doi.org/10.1021/acsnano.3c09878
ACS Nano 2024, 18, 9929−9941